

Hot deformation characteristics of Incoloy 926 super-austenitic stainless steel

Q. D. Nie¹, G. Yang², X. Wang^{1*}, C. Qin¹, X. L. Li¹, N. X. Li³

¹Key Laboratory of Superlight Material and Surface Technology, Ministry of Education, Harbin Engineering University, Harbin 150001, P. R. China

²School of Chinese Language and Culture, Tianjin University of Technology, Tianjin 300384, P. R. China

³Yantai Branch of China North Industries Group Corporation No. 52 Institute Co., Ltd., Ningbo Branch of Chinese Academy of Ordnance Science, Yantai 264000, P. R. China

Received 22 August 2019, received in revised form 20 December 2019, accepted 14 May 2020

Abstract

The deformation behavior of the Incoloy 926 super-austenitic stainless steel at 1000–1150 °C and 0.001–10 s⁻¹ was investigated. The corrected true stress-true strain curves were obtained by compensating the interfacial friction in the flow stress-strain curves. The interfacial friction increased the flow stress, and this increase was more pronounced at higher strains. According to the constitutive model, the activation energy varied from 328 to 384 kJ mol⁻¹ with respect to strain. The mechanical parameters, peak stress and peak strain, critical stress and critical strain, were described by clearer equations with the temperature and strain rate. Moreover, based on the processing maps and the microstructural observation, the unsafe deformation domain where the localized plastic flow occurred was validated at above 1 s⁻¹, the favorable process at 1100 °C and 0.1 s⁻¹ where fine and homogeneous grains can be obtained was determined simultaneously.

Key words: super-austenitic stainless steel, hot deformation, constitutive model, processing maps

1. Introduction

The International Stainless Steel Forum (ISSF) has released figures for the full year 2018 showing that 50.7 million metric tons of stainless steel were produced, more than 75 % was traditional austenitic stainless steel (200-series and 300-series). Austenitic stainless steel was widely applied in power and energy fields where corrosion resistance is mandatory [1]. However, when superior corrosion resistance is required at higher pressure and temperature, super-austenitic stainless steel is particularly interesting. Incoloy 926 alloy is a super austenitic stainless steel (SASS) and in compliance with ASME, which shows more outstanding corrosion resistance and thermal stability than traditional austenitic steel and is a potential substitute [2–4]. Incoloy 926 alloy products are generally fabricated by hot rolling or extrusion. The microstructure after hot deformation has an important effect on the

final mechanical properties of the steel.

In general, different kinds of microstructural evolution phenomenon, such as work hardening, dynamic recovery (DRV) and dynamic recrystallization (DRX), occur and interact during hot deformation [5–7]. Thus, it is useful for us to have a proper constitutive model to predict and understand the hot deformation behavior. In the past decades, several models have been proposed to describe the hot deformation process, for example, Mechanical Threshold Stress (MTS) model [8], Johnson-Cook (JC) model [9], Zerilli-Armstrong (ZA) model [10, 11], and Arrhenius-type constitutive model [12]. Nevertheless, the Arrhenius-type constitutive model is most common due to less experimental requirement and fewer material constants. For the Arrhenius-type model, the flow stress is only related to the temperature and strain rate but takes no consideration of the variable stress response to strain. In order to improve the accuracy, a strain-dependent pa-

*Corresponding author: tel.: +86 451 82569890; e-mail address: wangxiang@hrbeu.edu.cn

Table 1. Chemical composition of Incoloy 926 alloy (wt.%)

C	Si	Mn	P	Cr	N	Mo	Ni	Cu	Fe
0.02	0.40	1.30	0.02	19.50	0.21	6.25	24.72	0.84	46.74

parameter was introduced to compensate the Arrhenius model recently [13, 14].

To explicitly describe the evolutionary mechanism of microstructure and distinguish the intrinsic workability response to the deformation parameters, the process maps were constructed based on the dynamic materials model (DMM) proposed by Prasad et al., which comprises a superimposition of power dissipation and instability maps [15–18]. Typically, the deformation condition with high efficiency of power dissipation and flow stability is chosen as the favorable working parameter, which has been corroborated well with different alloys, e.g., super-austenitic stainless steel [19], Ni-based superalloy [20], magnesium alloy [21], and titanium alloy [22].

In the present paper, isothermal hot compression tests of Incoloy 926 alloy were performed at different temperatures and strain rates on a Gleeble-3800 thermal-simulation machine. The effect of friction at the anvil-workpiece interface on the stress was analyzed by compensating the stress-strain curves. The strain corrected Arrhenius model was adopted to describe the mechanical behavior of hot deformation. The processing maps constructed by DMM were developed to analyze the hot workability with the supplement of associated microstructure observation.

2. Experiment

The chemical composition of Incoloy 926 alloy used in this study is listed in Table 1. The cylindrical specimens were machined with the dimension of $\varnothing 8 \times 12 \text{ mm}^2$ for hot compression on a Gleeble-3800 thermo-simulation machine. The graphite and tantalum foils were used to minimize the friction at the anvil-workpiece interface. The specimens were firstly heated up to 1200°C at a heating rate of 10°C s^{-1} and held for 3 min to obtain homogeneous microstructure, secondly cooled to the desired temperature (1000, 1050, 1100, and 1150°C) at a cooling rate of 10°C s^{-1} and held for 2 min, thirdly deformed to 0.65 strain at a constant rate (0.001, 0.01, 0.1, 1, and 10 s^{-1}). Finally, the deformed specimens were quenched in water to room temperature immediately.

The quenched specimens were bisected along the compression direction. The cut surface was mechanically polished and etched in blue copperas (5 g), muriatic acid (20 ml), and water (20 ml) for the microstruc-

ture observation performed by Leic DMILM optical metallurgical microscopy. The ImageJ software was used to evaluate the grain diameter distribution. Additionally, Vickers hardness measurements were carried out at the polished surfaces, using a load of 300 g and a dwell time of 10 s.

3. Results and discussion

3.1. Flow stress curves and friction correction

The compression pressure was affected by many factors, including the converted heat from deformation and the friction at the anvil-workpiece interface. The converted heat can soften the specimen and decrease the flow stress. However, the thermocouple at the specimen surface recorded that the fluctuation of temperature was kept in the range of $\pm 3^\circ\text{C}$ during deformation, which validated that the converted heat had been dissipated by radiation and convection through the anvils. Consequently, the influence of converted energy can be ignored. During compression tests, the sample will spread over the anvils to increase its diameter with the decreasing height. The interfacial friction opposed the outward flow of this metal, leading to increasing the resistance to deformation. Although tantalum and graphite foils were used in this research, there remained slight barreling on the edges of the specimens suggestive of the influence of the friction on the flow stress. To avoid the inaccuracy, the true stress-true strain curves should be corrected by taking the influence of the friction into account.

Dieter [23] proposed that the effect of friction on the flow stress can be expressed by:

$$\sigma = \frac{C^2 P}{2 [\exp(C) - C - 1]} \quad (1)$$

with

$$C = \frac{2\mu r}{h}, \quad (2)$$

where σ is the stress in the absence of friction, P is the flow stress of materials under frictional conditions, r and h are the radius and height of the specimen, μ is the friction coefficient. μ can be calculated by the following equation [24]:

$$\mu = \frac{(R/h)}{(4/\sqrt{3}) - (2b/3\sqrt{3})} \quad (3)$$

with

$$b = 4 \frac{\Delta R}{R} \frac{h}{\Delta h}. \quad (4)$$

In the preceding Eq. (4), b is the barreling factor, ΔR is the difference between the maximum and minimum

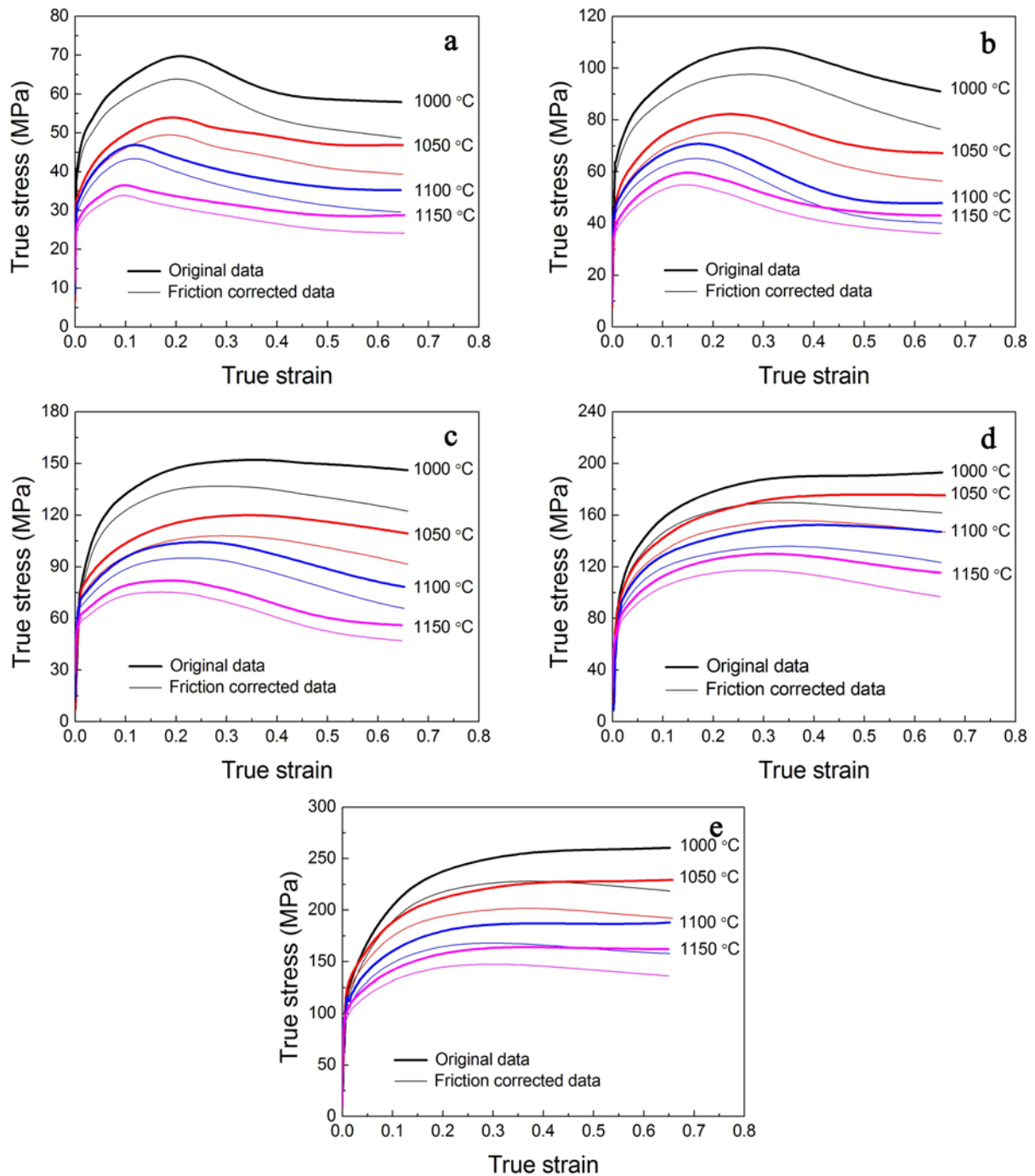


Fig. 1. The original and friction corrected true stress-true strain curves of the studied steel at different temperatures and strain rates of (a) 0.001 s^{-1} , (b) 0.01 s^{-1} , (c) 0.1 s^{-1} , (d) 1 s^{-1} , and (e) 10 s^{-1} .

radii of the specimen, R is the theoretical radius after homogeneous deformation (postulating that the specimen keeps the volume constant), h is the final height, and Δh is the difference between initial and final heights of the specimen.

The original and friction corrected true stress-true strain curves of the Incoloy 926 alloy at different deformation temperatures and strain rates are illustrated in Fig. 1. It is shown that the interfacial friction increases

the flow stress, and this increase is more pronounced at higher strains. The phenomena result from the coefficient of friction and the increasing surface of the specimen in contact with dies. All experimental flow curves in Fig. 1 show similar characteristics before the peak.

Rapidly increasing stress is detected at the initial deformation stage due to the rapidly increasing number of dislocation [25, 26]. Following the above stage,

the increasing rate of flow stress decreases gradually, resulting from DRV and DRX partially counteracting the effect of work hardening simultaneously [27]. The flow stress increases no more when the work hardening and the dynamic softening (caused by DRV and DRX) were in balance, and the peak was thus achieved. But the curves show two different tendencies after the peak. The first type shows subsequent decreasing flow stress, resulting from the predominant dynamic softening. Further, several curves at high temperature and low strain rate reach the steady-state at 0.65 strain, which indicates that the work hardening rate is equal to the dynamic softening rate again, e.g., in Fig. 1a. The second type curves exhibit a broadened peak with subsequent constant flow stress, e.g., in Fig. 1e. Generally, the curves with weak or no peak are considered to be associated with DRV. Still, some researchers [28, 29] have demonstrated that slight DRX could also occur and was observed in this studied steel in section 3.4.

For constant strain, the curves move to higher flow stress with increasing strain rate and decreasing deformation temperature, which also proves that the stress is sensitive to both deformation parameters. Such a phenomenon can be explained by the following two aspects. On the one hand, the thermally-activated cross-slip and climb of dislocation can take place at high temperature easily, which accelerates the occurrence of dynamic softening, resulting in decreasing the flow stress [30]; on the other hand, the dislocation accumulates rapidly in a short time at high strain rate, which will promote the work hardening, resulting in increasing the flow stress [31].

3.2. Constitutive analysis

The correlation between the flow stress, strain rate, and deformation temperature can be modeled by the following power function (Eq. (5)), the exponential function (Eq. (6)), and the hyperbolic sine function (Eq. (7)) [32]:

$$Z = \dot{\epsilon} \exp(Q/RT) = A_1 \sigma^{n_1}, \quad \alpha\sigma < 0.8, \quad (5)$$

$$Z = \dot{\epsilon} \exp(Q/RT) = A_2 \exp(n_2\sigma), \quad \alpha\sigma < 1.2, \quad (6)$$

$$Z = \dot{\epsilon} \exp(Q/RT) = A [\sinh(\alpha\sigma)]^n, \quad \text{for all } \sigma, \quad (7)$$

where Z is the Zener-Hollomon parameter, $\dot{\epsilon}$ is the strain rate (s^{-1}), Q is the activation energy for hot deformation (J mol^{-1}), R is the gas constant ($8.314 \text{ J mol}^{-1} \text{ K}^{-1}$), σ is the flow stress (MPa), T is the absolute temperature (K), A_1 , A_2 , A , n_1 , n_2 , n , and α ($\approx n_2/n_1$) are the material constants.

Taking the natural logarithm from each side of Eqs. (5)–(7) yields to the following equations:

$$\ln \dot{\epsilon} = \ln A_1 - Q/RT + n_1 \ln \sigma, \quad (8)$$

$$\ln \dot{\epsilon} = \ln A_2 - Q/RT + n_2 \sigma, \quad (9)$$

$$\ln \dot{\epsilon} = \ln A - Q/RT + n \ln [\sinh(\alpha\sigma)]. \quad (10)$$

For a constant temperature, by partial differentiation of Eqs. (8)–(10), n_1 , n_2 , and n can be derived as:

$$n_1 = \left. \frac{\partial \ln \dot{\epsilon}}{\partial \ln \sigma} \right|_T, \quad (11)$$

$$n_2 = \left. \frac{\partial \ln \dot{\epsilon}}{\partial \sigma} \right|_T, \quad (12)$$

$$n = \left. \frac{\partial \ln \dot{\epsilon}}{\partial \ln [\sinh(\alpha\sigma)]} \right|_T. \quad (13)$$

For a constant strain rate, by partial differentiation of Eq. (10), Q can be derived as:

$$Q = Rn \left. \frac{\partial \ln [\sinh(\alpha\sigma)]}{\partial (1/T)} \right|_{\dot{\epsilon}}. \quad (14)$$

Once n_1 and n_2 are calculated by measuring the reciprocal of the slope of $\ln \sigma$ – $\ln \dot{\epsilon}$ and σ – $\ln \dot{\epsilon}$, α can be obtained. According to Eqs. (13) and (14), the values of n and Q can be determined subsequently.

Based on Eqs. (11) and (12), the illustration of $\ln \sigma$ – $\ln \dot{\epsilon}$ and σ – $\ln \dot{\epsilon}$ is presented in Figs. 2a,b at 0.2 strain, the average of n_1 and n_2 were determined as 6.519 and 0.0678, respectively. Thus, α was obtained as 0.0104. The diagrams of n and Q are plotted in Figs. 2c,d, and the values of them were calculated as 4.83 and 332 kJ mol^{-1} . By importing Q , R , and $\dot{\epsilon}$ into Eq. (5), Z was also obtained.

Taking the natural logarithm of Eq. (7), Eq. (15) can be obtained:

$$\ln Z = \ln A + n \ln [\sinh(\alpha\sigma)]. \quad (15)$$

By importing the calculated n , a , and Q , the plot of $\ln Z$ – $n \ln [\sinh(\alpha\sigma_p)]$ is shown in Fig. 3. After line regression analysis, the value of A is derived as 2.55×10^{11} from the intercept of a fitting line. The adjusted coefficient was 0.9955, which demonstrates the high accuracy of material constants for describing the flow stress.

The Eq. (7) can also be expressed in the following:

$$\dot{\epsilon} = A [\sinh(\alpha\sigma)]^n \exp(-Q/RT). \quad (16)$$

By inputting the relative A , α , n , and Q into Eq. (16), the Arrhenius constitutive model of this steel at 0.2 strain can be expressed as:

$$\dot{\epsilon} = 2.55 \times 10^{11} [\sinh(0.0104\sigma)]^{4.83} \cdot \exp(-332000/RT). \quad (17)$$

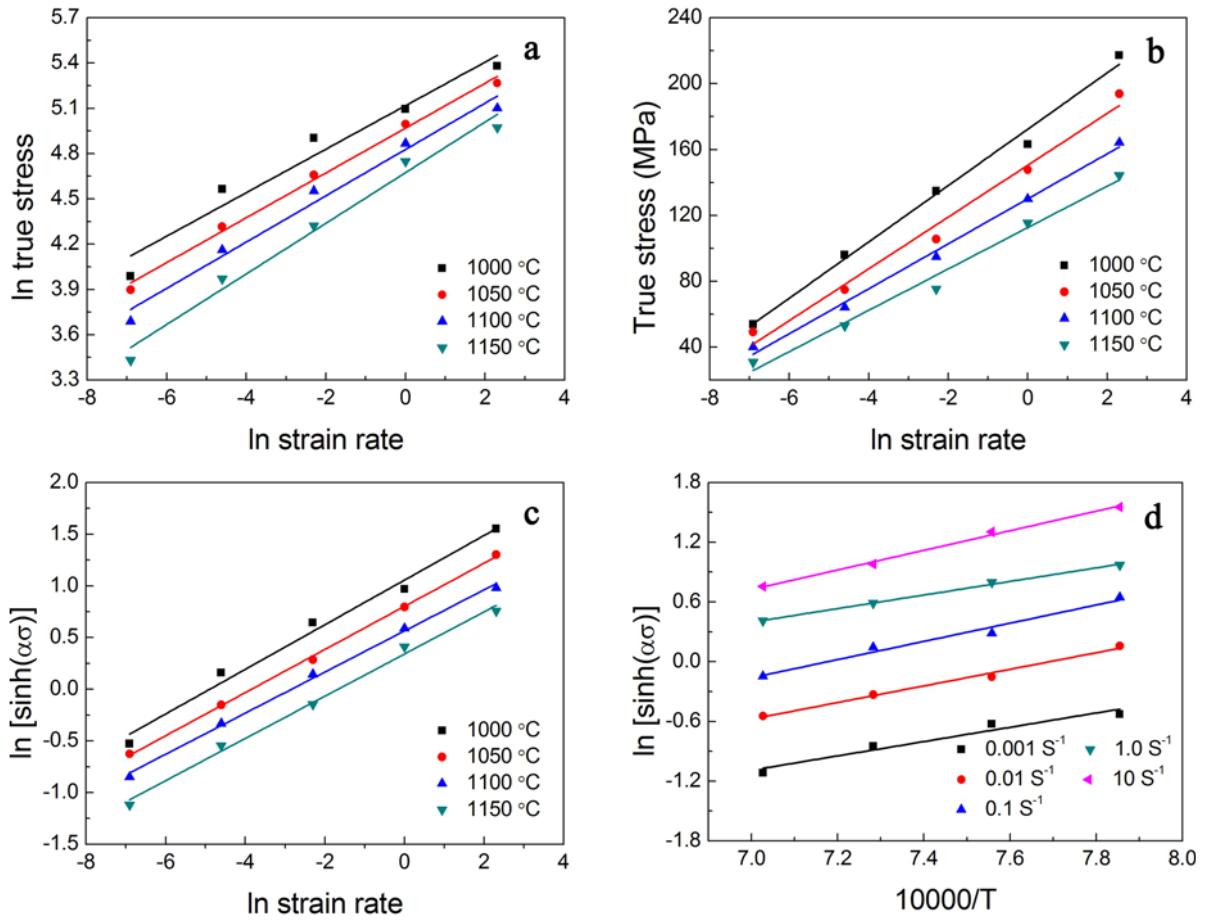


Fig. 2. The plots showing the determination of (a) n_1 , (b) n_2 , (c) n , and (d) Q .

The flow stress at 0.2 strain can also be represented as a function of the Z parameter, i.e.:

$$\begin{aligned} \sigma &= \frac{1}{\alpha} \left\{ \left(\frac{Z}{A} \right)^{\frac{1}{n}} + \left[\left(\frac{Z}{A} \right)^{\frac{2}{n}} + 1 \right]^{\frac{1}{2}} \right\} \\ &= \frac{1}{0.0104} \ln \left\{ \left(\frac{Z}{2.55 \times 10^{11}} \right)^{\frac{1}{4.83}} \right. \\ &\quad \left. + \left[\left(\frac{Z}{2.55 \times 10^{11}} \right)^{\frac{2}{4.83}} + 1 \right]^{\frac{1}{2}} \right\}. \end{aligned} \quad (18)$$

The above Eqs. (17), (18) take no consideration of the effect of strain level on the flow stress. In fact, the flow stress changes with the variable strain due to the inverse mechanisms, the work hardening and dynamic softening. Thus, the revised constitutive model considering the effect of strain was developed, which has been employed to give accurate prediction [14]. According to the abovementioned calculation process, the material constants (α , Q , n , and A) at different strains ranging from 0.1 to 0.6, with an interval of 0.05 were calculated and illustrated in Fig. 4. The re-

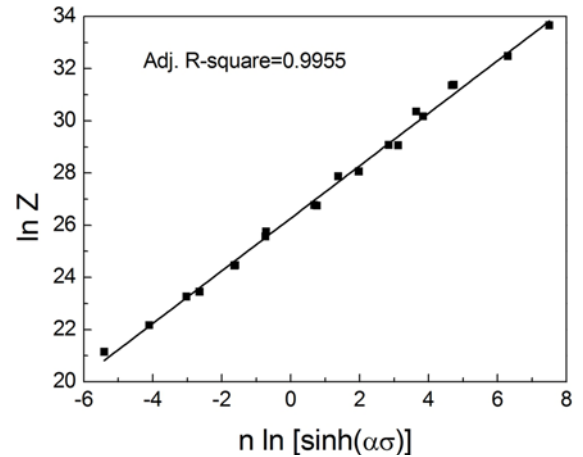


Fig. 3. Relationship between $\ln Z$ and $n \ln \sinh(\alpha\sigma)$.

lationship between material constants and strains was obtained by a third-order polynomial fitting as follows:

$$\alpha = 0.01244 - 0.02019\varepsilon + 0.05815\varepsilon^2 - 0.0454\varepsilon^3, \quad (19)$$

$$n = 6.1086 - 7.4947\varepsilon + 7.4709\varepsilon^2 - 1.2277\varepsilon^3, \quad (20)$$

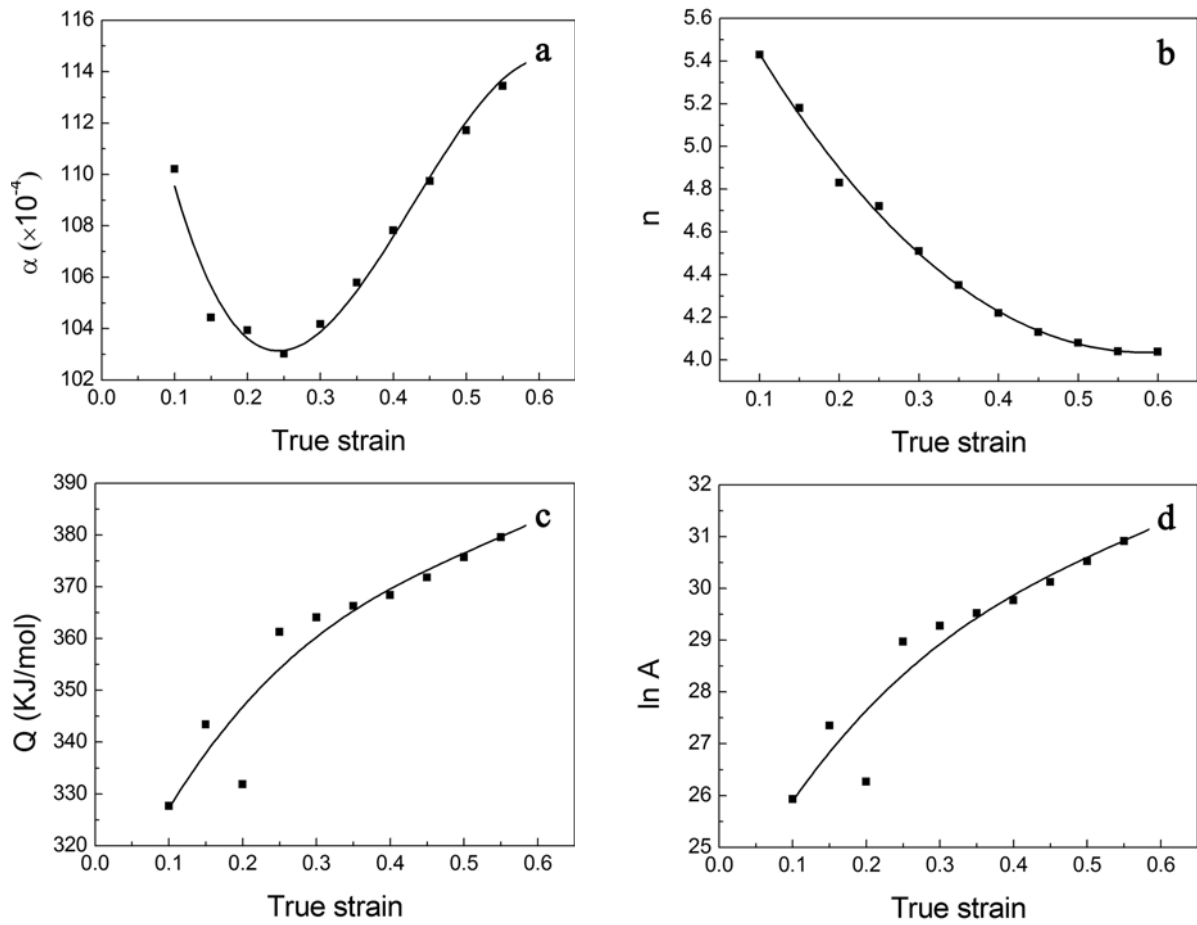


Fig. 4. Variation of material parameters with increasing strain.

$$Q/1000 = 299.795 + 320.188\varepsilon - 487.618\varepsilon^2 + 308.095\varepsilon^3, \quad (21)$$

$$\ln A = 23.5609 + 26.7079\varepsilon - 35.6844\varepsilon^2 + 20.8454\varepsilon^3. \quad (22)$$

3.3. Kinetic model of DRX

The critical stress (σ_c), critical strain (ε_c), peak stress (σ_p), and peak strain (ε_p) are four important mechanical characteristic parameters for the description of hot deformation. σ_p and ε_p can be determined by the curves directly, but the critical ones can not. Poliak and Jonas [33, 34] proposed that σ_c and ε_c could be obtained by the minimum in the absolute value of strain hardening slope which was calculated from strain hardening rate ($\theta = \partial\sigma/\partial\varepsilon$) versus flow stress curves. This method has been used by many researchers successfully [35, 36]. In the present investigation, the value of σ_c was obtained by plotting the strain hardening rate concerning true stress. To identify the value of σ_c directly, the double-differentiation technique was employed, and the point at which the $\partial^2\theta/\partial\sigma^2 = 0$ was determined as the σ_c . The diagrams of θ - σ and $\partial\theta/\partial\sigma$ - σ at 1150°C and different strain

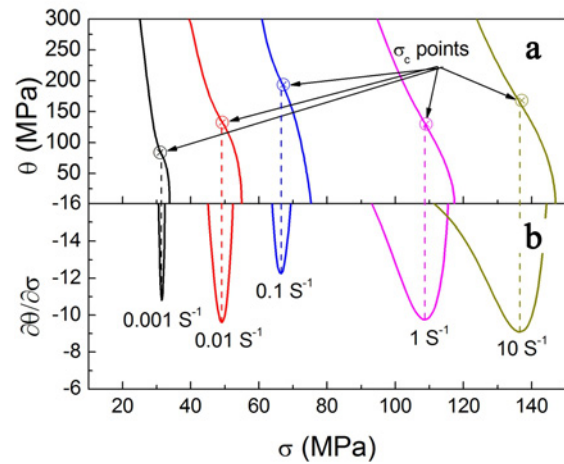


Fig. 5. (a) Work hardening curves of the specimens deformed and (b) the derivative of the θ - σ plot under 1150°C and different strain rates.

rates are presented in Fig. 5. As observed, θ gradually decreases with the increasing stress because of the occurrence of DRV at the initial stage, until a downward inflexion point, σ_c , appears, after which the decreas-

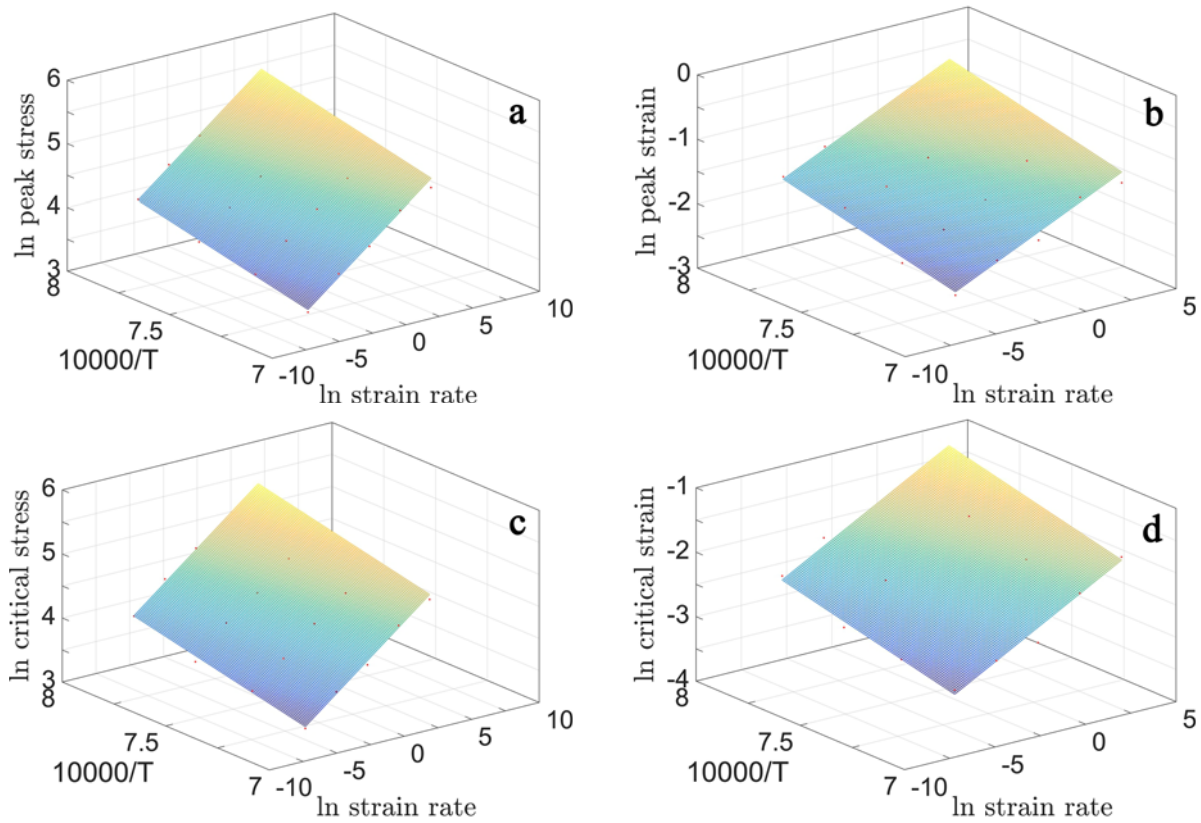


Fig. 6. Dependence of (a) σ_p , (b) σ_c , (c) ε_p , and (d) ε_c on temperature and strain rate.

ing rate of θ increases gradually due to the influence of DRX. The other critical stresses under different deformation conditions were obtained as the same method above.

Junior and Balancin [37] considered that the mechanical parameters (σ_p , σ_c , ε_p , and ε_c) could be described by following power-law equation:

$$\text{Parameter} = 10^{[a \log(Z)+b]}, \quad (23)$$

where a and b are material constants. This conclusion has also been proved by Zhang et al. [38]. To reveal the dependence of mechanical parameters on deformation conditions (the temperature and strain rate) directly, we took the natural logarithm of both sides of a new equation which was obtained by combining Eqs. (5) and (23), a clearer description of the relationship between the flow parameters and the deformation conditions was obtained as follows:

$$\ln \text{Parameter} = b \ln 10 + a \ln \dot{\varepsilon} + aQ/RT. \quad (24)$$

In Eq. (24), the Q is usually determined by peak stress which is thought to be related to the deformation mechanism and useful for industrial processes [38, 39]. Figure 6 shows the values of mechanical parameters with respect to $\ln \dot{\varepsilon}$ and $1/T$. Furthermore, the regression analysis of the data demonstrates the rela-

tionship between them in the following forms:

$$\ln \sigma_p = -0.165 + 0.1709 \ln \dot{\varepsilon} + 6992/T, \quad (25)$$

$$\ln \sigma_c = -0.3552 + 0.1713 \ln \dot{\varepsilon} + 7137/T, \quad (26)$$

$$\ln \varepsilon_p = -6.511 + 0.1314 \ln \dot{\varepsilon} + 7360/T, \quad (27)$$

$$\ln \varepsilon_c = -7.405 + 0.1558 \ln \dot{\varepsilon} + 7677/T. \quad (28)$$

It is clearly shown in Fig. 6 that all values of the mechanical parameters increase with the decreasing deformation temperature and increasing strain rate.

3.4. Processing maps

According to DMM, the correlation between the flow stress and strain rate can be expressed by the following equation [40]:

$$\sigma = K \dot{\varepsilon}^m, \quad (29)$$

where σ is the flow stress (MPa), $\dot{\varepsilon}$ is the strain rate (s^{-1}), m is the strain rate sensitivity of flow stress, and K is a constant related with the condition of hot deformation.

The total power (P) absorbed during the deformation process consists of two complementary portions:

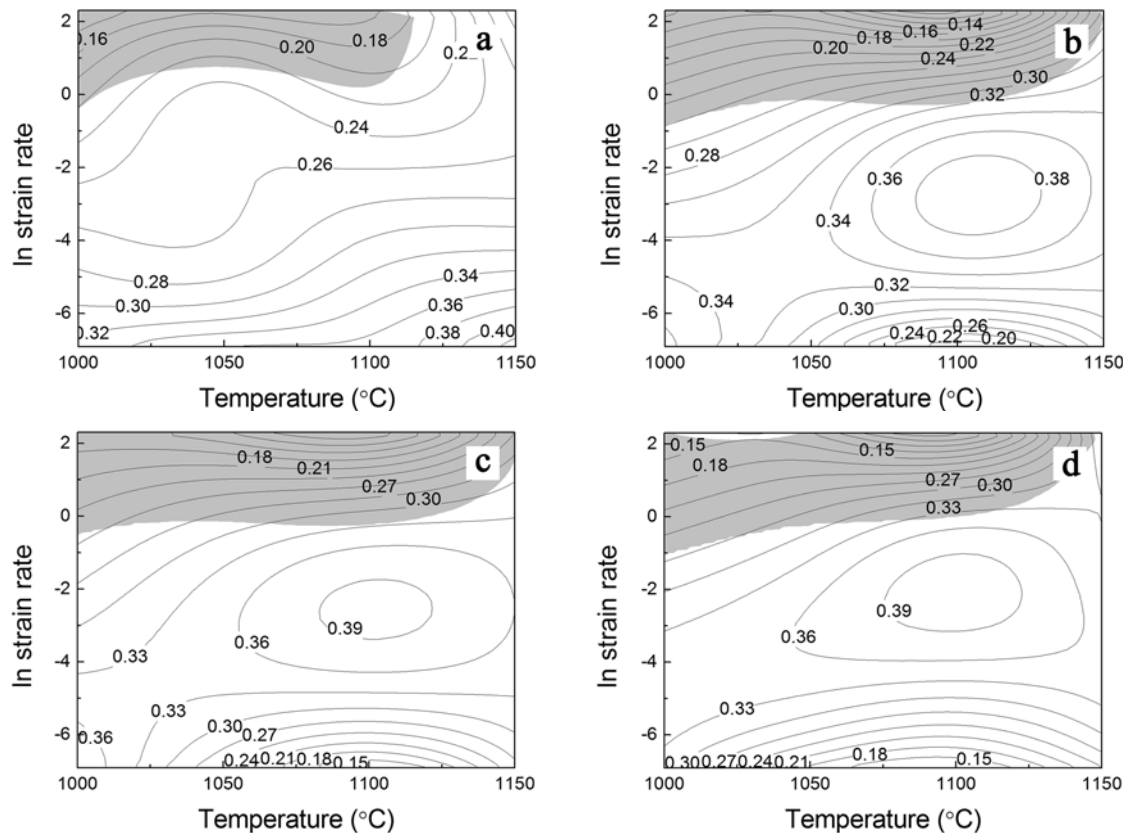


Fig. 7. Processing maps for the specimens at strains of (a) 0.2, (b) 0.4, (c) 0.5, and (d) 0.6.

the dissipative power (G) which is the dissipative energy of the material plastic deformation, and the dissipation of association (J) which is the dissipative energy of the microstructure evolution [41]:

$$P = \sigma \dot{\varepsilon} = \int_0^{\dot{\varepsilon}} \sigma d\dot{\varepsilon} + \int_0^{\sigma} \dot{\varepsilon} d\sigma = G + J, \quad (30)$$

where G and J depend on the strain rate sensitivity of flow stress (m) in Eq. (29). The power constituent that is related to microstructure evolution can be normalized by postulating the specimen as an ideal linear dissipater [15, 42]. The efficiency of power dissipation (η) was introduced and defined as:

$$\eta = \frac{J}{J_{\max}} = \frac{2m}{m+1} \quad (31)$$

and m was given in the following:

$$m = \left. \frac{\partial \ln \sigma}{\partial \ln \dot{\varepsilon}} \right|_{\varepsilon, T}, \quad (32)$$

where the η reveals the proportion of energy dissipated in structural transformation, whose contour plot on the temperature-strain rate coordinate area makes up

of the power dissipation map. Different regions of the map represent the specific microstructural process and can be applied to predict microstructure evolution.

To evaluate the deformation capacity, a non-dimensional instability parameter, $\xi(\dot{\varepsilon})$, was introduced and expressed by [41]:

$$\xi(\dot{\varepsilon}) = \frac{\partial \ln [m/(m+1)]}{\partial \ln \dot{\varepsilon}} + m < 0. \quad (30)$$

The $\xi(\dot{\varepsilon})$ is negative when flow instability occurs. The variation of $\xi(\dot{\varepsilon})$ with deformation temperature and strain rate constitutes the instability map. By overprinting the instability map on the power dissipation map, the processing map can be constructed, which can be utilized to obtain the favorable parameters in the high η and positive $\xi(\dot{\varepsilon})$.

The processing maps of this steel at the temperature range of 1000–1150°C, strain rate range of 0.001–10 s⁻¹, and strain range of 0.2–0.6 are shown in Fig. 7. The contour numbers are consistent with the power dissipation efficiency in Eq. (28). All grey regions mean that $\xi(\dot{\varepsilon})$ is negative, and it is unsafe to compress at these conditions. The precise power dissipation efficiency is changing gradually and regularly, which exhibits the significant influence of the strain. Although the peak dissipation efficiency is nearly constant at different strains, the high dissipation efficiency domain moves from the location in 1150°C and

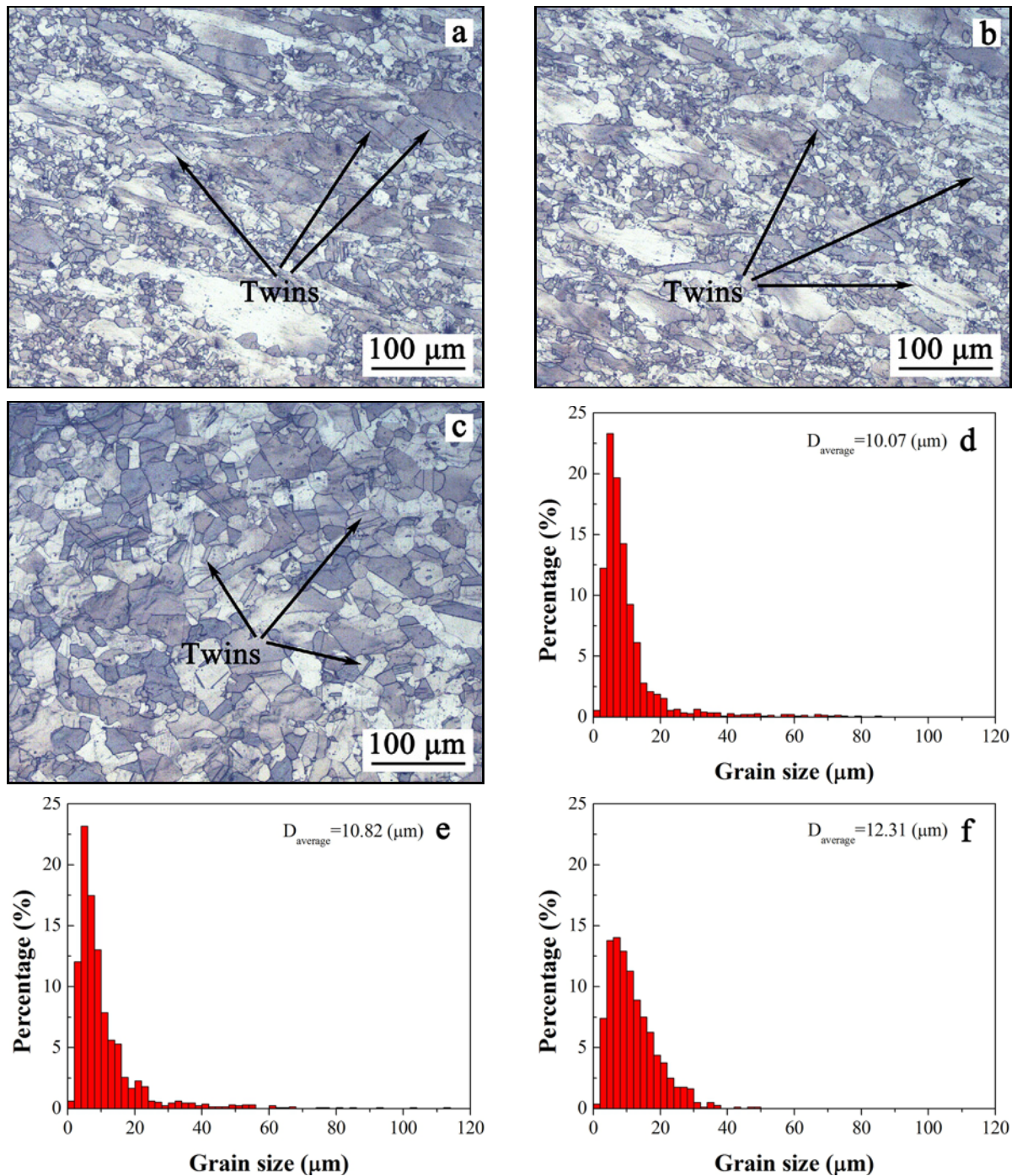


Fig. 8. The optical microstructure and grain diameter distribution of the studied steel deformed to 0.6 strain at (a, d) 1000°C, 10 s⁻¹; (b, e) 1100°C, 10 s⁻¹; and (c, f) 1100°C, 0.1 s⁻¹.

0.001 s⁻¹ at the strain of 0.2 to that in 1100°C and 0.1 s⁻¹ at 0.4, 0.5, and 0.6 strain. The unsafe region always locates at low temperature and high strain rate but shows a different area with the increasing strain. The detailed show reveals that the grey domain covers from 1000°C to 1100°C at above 1 s⁻¹ at 0.2 strain, and extends to almost the entire testing temperature at strain rates of above 0.1 s⁻¹ at 0.4, 0.5, and 0.6 strain with a similar area.

To verify the applicability of the processing maps, several selected specimens deformed to 0.6 strain at unsafe region (1000°C, 10 s⁻¹ and 1100°C, 10 s⁻¹) and high dissipation efficiency region (1100°C, 0.1 s⁻¹) were machined parallel to the compression direction for microstructure observation. As indicated in Fig. 8, some twins appear in the interior of partial grains. The twins generated during hot deformation played an important role in bulging and accelerating the separation

of the bulged parts from the original grains, which favored the nucleation and development of DRX grains [43].

Also, the microstructure with original grains and fine DRX grains can be observed in Figs. 8a,b. The original grains are extended along about 45° angle to the compression direction, and large quantities of serration and bulges appear on their boundaries. The shell of fine DRX grains is formed around pre-existing grain boundaries (necklace structure), which denotes that DRX can also be triggered by the typical necklace mechanism [44]. The formation of the necklace structure is attributed to the following reasons. Once the rapid deformation starts, a lot of slip bands move to the grain boundaries and are closely packed, resulting in high dislocation density and the localized plastic flow occurring. Adiabatic deformation heat failed to conduct for a short time, leading to a temperature rise in the local flow regions, thereby facilitating recrystallization nucleation along these parts. These factors finally result in the occurrence of DRX along grain boundaries [45]. Figures 8d,e show the grain diameter distribution with respect to Figs. 8a,b, respectively. It is observed that most of the grain size is less than $40\ \mu\text{m}$, but there are still several large grains with the maximum $112\ \mu\text{m}$ at 1000°C and $10\ \text{s}^{-1}$ with the maximum $85\ \mu\text{m}$ at 1100°C and $10\ \text{s}^{-1}$. These large grains belong to the original grains elongated during deformation. The DRX fine grains and large elongated grains compose a mixed crystal structure which is detrimental to the mechanical properties consistency within a component and should be avoided during hot working process. Moreover, the localized plastic flow is generally considered as an unsafe deformation mechanism [16].

The microstructure and grain diameter distribution of the specimen deformed in high dissipation efficiency domain, 1100°C and $0.1\ \text{s}^{-1}$, is exhibited in Figs. 8c,f. The equiaxed grains with wavy or corrugated boundaries constitute the whole microstructure. The average size is $12.31\ \mu\text{m}$, more than 99% are less than $40\ \mu\text{m}$. According to the grain morphology and size distribution, we can confirm that the deformation mechanism in this region was dominated by DRX. Compared with $183.9\ \text{HV}$ of the undeformed specimens, the measured Vickers microhardness of the specimen deformed at this condition reaches to $220.9\ \text{HV}$, which has been enhanced by $37\ \text{HV}$. The increase of hardness values is related to the grain refinement. As we all know, the refined grains are favorable for the strength and toughness, which is also one of the purposes of hot deformation. Based on the above analysis, 1100°C and $0.1\ \text{s}^{-1}$ can be considered as the highly desirable and excellent parameters during hot deformation of this steel.

4. Conclusions

In this investigation, the deformation behavior and dynamic recrystallization of the Incoloy 926 alloy have been researched by hot deformation tests at $1000\text{--}1150^\circ\text{C}$ and $0.001\text{--}10\ \text{s}^{-1}$. The following conclusions are drawn:

1. The corrected true stress-true strain curves were obtained by compensating the interfacial friction in the flow stress-strain curves. The interfacial friction increased the flow stress, and this increase was more pronounced at higher strains.

2. Based on the revised constitutive model, the deformation activation energy was calculated and varied from 328 to $384\ \text{kJ mol}^{-1}$ along with relative strain.

3. The mechanical parameters σ_p , ε_p , σ_c , and ε_c were described by clearer equations with the temperature and strain rate.

4. According to the processing map and microstructural observation at 0.6 strain, the flow instability domain was determined at above $0.1\ \text{s}^{-1}$, with mixed crystal structure which was detrimental to the mechanical property consistency. Simultaneously, the refined DRX structure can be obtained at the favorable parameters, 1100°C and $0.1\ \text{s}^{-1}$.

Acknowledgement

The authors would like to acknowledge the financial support of the Fundamental Research Funds for the Central Universities (HEUCFP201727).

References

- [1] B. Wang, M. Y. Jiang, M. Xu, C. W. Cui, J. Wang, W. Q. Cheng, Influence of heat treatment on corrosion resistance of explosive welding 316L stainless steel composite plate, *Mater. Res. Express* 6 (2019) 106575. [doi:10.1088/2053-1591/ab358e](https://doi.org/10.1088/2053-1591/ab358e)
- [2] G. Mori, M. Prohaska, R. Lackner, K. Rokosz, M. Albu, G. Kothleitner, Depletion zones and intergranular corrosion of superaustenitic stainless steel Alloy 926, *Mater. Corros.* 68 (2017) 284–294. [doi:10.1002/maco.201609152](https://doi.org/10.1002/maco.201609152)
- [3] R. Leiva-García, M. J. Muñoz-Portero, J. García-Antón, Evaluation of Alloy 146, 279, 900, and 926 sensitization to intergranular corrosion by means of electrochemical methods and image analysis, *Corros. Sci.* 51 (2009) 2080–2091. [doi:10.1016/j.corsci.2009.05.036](https://doi.org/10.1016/j.corsci.2009.05.036)
- [4] R. Leiva-García, R. Akid, D. Greenfield, J. Gittens, M. J. Muñoz-Portero, J. García-Antón, Study of the sensitization of a highly alloyed austenitic stainless steel, Alloy 926 (UNS N08926), by means of scanning electrochemical microscopy, *Electrochim. Acta* 70 (2012) 105–111. [doi:10.1016/j.electacta.2012.03.036](https://doi.org/10.1016/j.electacta.2012.03.036)
- [5] A. Dehghan-Manshadi, M. Barnett, P. D. Hodgson, Hot deformation and recrystallization of austenitic

- stainless steel: Part I. Dynamic recrystallization, *Metall. Mater. Trans. A* 39 (2008) 1359–1370. [doi:10.1007/s11661-008-9512-7](https://doi.org/10.1007/s11661-008-9512-7)
- [6] A. M. Wusatowska-Sarnek, H. Miura, T. Sakai, Nucleation and microtexture development under dynamic recrystallization of copper, *Mater. Sci. Eng. A* 323 (2002) 177–186. [doi:10.1016/S0921-5093\(01\)01336-3](https://doi.org/10.1016/S0921-5093(01)01336-3)
- [7] G. R. Ebrahimi, A. Zarei-Hanzaki, H. Arabshahi, The effect of strain rate variations on the microstructure and hot deformation behaviour of AA2024 aluminium alloy, *Kovove Mater.* 46 (2008) 229–233.
- [8] P. S. Follansbee, U. F. Kocks, A constitutive description of the deformation of copper based on the use of the mechanical threshold stress as an internal state variable, *Acta Metall.* 36 (1988) 81–93. [doi:10.1016/0001-6160\(88\)90030-2](https://doi.org/10.1016/0001-6160(88)90030-2)
- [9] G. R. Johnson, W. H. Cook, Fracture characteristics of three metals subjected to various strains, strain rates, temperatures and pressures, *Eng. Fract. Mech.* 21 (1985) 31–48. [doi:10.1016/0013-7944\(85\)90052-9](https://doi.org/10.1016/0013-7944(85)90052-9)
- [10] F. J. Zerilli, R. W. Armstrong, Dislocation-mechanics-based constitutive relations for material dynamics calculations, *J. of Appl. Phys.* 61 (1987) 1816–1825. [doi:10.1063/1.338024](https://doi.org/10.1063/1.338024)
- [11] D. Samantaray, S. Mandal, A. K. Bhaduri, A comparative study on Johnson Cook, modified Zerilli-Armstrong and Arrhenius-type constitutive models to predict elevated temperature flow behaviour in modified 9Cr-1Mo steel, *Comput. Mater. Sci.* 47 (2009) 568–576. [doi:10.1016/j.commatsci.2009.09.025](https://doi.org/10.1016/j.commatsci.2009.09.025)
- [12] C. M. Sellars, W. J. McTegart, On the mechanism of hot deformation, *Acta Metall.* 14 (1966) 1136–1138. [doi:10.1016/0001-6160\(66\)90207-0](https://doi.org/10.1016/0001-6160(66)90207-0)
- [13] C. Y. Sun, G. Liu, Q. D. Zhang, R. Li, L. L. Wang, Determination of hot deformation behavior and processing maps of IN 028 alloy using isothermal hot compression test, *Mater. Sci. Eng. A* 595 (2014) 92–98. [doi:10.1016/j.msea.2013.10.051](https://doi.org/10.1016/j.msea.2013.10.051)
- [14] L. Xu, L. Chen, G. J. Chen, M. Q. Wang, Hot deformation behavior and microstructure analysis of 25Cr3Mo3NiNb steel during hot compression tests, *Vacuum* 147 (2018) 8–17. [doi:10.1016/j.vacuum.2017.10.017](https://doi.org/10.1016/j.vacuum.2017.10.017)
- [15] Y. V. R. K. Prasad, H. L. Gegel, S. M. Doraivelu, J. C. Malas, J. T. Morgan, K. A. Lark, D. R. Barker, Modeling of dynamic material behavior in hot deformation: Forging of Ti-6242, *Metall. Trans. A* 15 (1984) 1883–1892. [doi:10.1007/BF02664902](https://doi.org/10.1007/BF02664902)
- [16] Y. Sun, W. D. Zeng, Y. Q. Zhao, X. M. Zhang, Y. Shu, Y. G. Zhou, Research on the hot deformation behavior of Ti40 alloy using processing map, *Mater. Sci. Eng. A* 528 (2011) 1205–1211. [doi:10.1016/j.msea.2010.10.019](https://doi.org/10.1016/j.msea.2010.10.019)
- [17] E. X. Pu, W. J. Zheng, J. Z. Xiang, Z. G. Song, H. Feng, Y. L. Zhu, Hot working characteristic of super-austenitic stainless steel 254SMO, *Acta Metall. Sin. (Engl. Lett.)* 27 (2014) 313–323. [doi:10.1007/s40195-014-0047-1](https://doi.org/10.1007/s40195-014-0047-1)
- [18] S. L. Guo, D. F. Li, H. J. Pen, Q. M. Guo, J. Hu, Hot deformation and processing maps of Inconel 690 superalloy, *J. Nucl. Mater.* 410 (2011) 52–58. [doi:10.1016/j.jnucmat.2010.12.309](https://doi.org/10.1016/j.jnucmat.2010.12.309)
- [19] E. X. Pu, W. J. Zheng, J. Z. Xiang, Z. G. Song, J. Li, Hot deformation characteristic and processing map of super-austenitic stainless steel S32654, *Mater. Sci. Eng. A* 598 (2014) 174–182. [doi:10.1016/j.msea.2014.01.027](https://doi.org/10.1016/j.msea.2014.01.027)
- [20] D. X. Wen, Y. C. Lin, H. B. Li, X. M. Chen, J. Deng, L. T. Li, Hot deformation behavior and processing map of a typical Ni-based superalloy, *Mater. Sci. Eng. A* 591 (2014) 183–192. [doi:10.1016/j.msea.2013.09.049](https://doi.org/10.1016/j.msea.2013.09.049)
- [21] N. Srinivasan, Y. V. R. K. Prasad, P. R. Rao, Hot deformation behaviour of Mg-3Al alloy — A study using processing map, *Mater. Sci. Eng. A* 476 (2008) 146–156. [doi:10.1016/j.msea.2007.04.103](https://doi.org/10.1016/j.msea.2007.04.103)
- [22] Y. H. Liu, Y. Q. Ning, Z. K. Yao, H. Z. Guo, Hot deformation behavior of Ti-6.0Al-7.0Nb biomedical alloy by using processing map, *J. Alloys Compd.* 587 (2014) 183–189. [doi:10.1016/j.jallcom.2013.10.132](https://doi.org/10.1016/j.jallcom.2013.10.132)
- [23] G. E. Dieter, *Mechanical Metallurgy*. New York, McGraw Hill Book Company 1976.
- [24] R. Ebrahimi, A. Najafizadeh, A new method for evaluation of friction in bulk metal forming, *J. Mater. Process. Technol.* 152 (2004) 136–143. [doi:10.1016/j.jmatprotec.2004.03.029](https://doi.org/10.1016/j.jmatprotec.2004.03.029)
- [25] K. Sumit, G. P. Chaudhari, S. K. Nath, Critical conditions for dynamic recrystallization of hot deformed 1 wt.% chromium – 1 wt.% molybdenum rotor steel, *Mater. Perform. Charact.* 8 (2019) 1032–1049. [doi:10.1520/MPC20190022](https://doi.org/10.1520/MPC20190022)
- [26] S. K. Rajput, G. P. Chaudhari, S. K. Nath, Characterization of hot deformation behavior of a low carbon steel using processing maps, constitutive equations and Zener-Hollomon parameter, *J. Mater. Process. Technol.* 237 (2016) 113–125. [doi:10.1016/j.jmatprotec.2016.06.008](https://doi.org/10.1016/j.jmatprotec.2016.06.008)
- [27] B. Kishor, G. P. Chaudhari, S. K. Nath, Hot deformation characteristics of 13Cr-4Ni stainless steel using constitutive equation and processing map, *J. Mater. Eng. Perform.* 25 (2016) 2651–2660. [doi:10.1007/s11665-016-2159-4](https://doi.org/10.1007/s11665-016-2159-4)
- [28] M. J. Luton, C. M. Sellars, Dynamic recrystallization in nickel and nickel-iron alloys during high temperature deformation, *Acta Metall.* 17 (1969) 1033–1043. [doi:10.1016/0001-6160\(69\)90049-2](https://doi.org/10.1016/0001-6160(69)90049-2)
- [29] Y. Mehta, S. K. Rajput, G. P. Chaudhari, V. V. Dabhade, Dynamic recrystallization and grain refinement of Fe-P-C-Si and Fe-P-C-Si-N steels, *J. Mater. Eng. Perform.* 27 (2018) 4770–4782. [doi:10.1007/s11665-018-3531-3](https://doi.org/10.1007/s11665-018-3531-3)
- [30] H. Miura, H. Aoyama, T. Sakai, Effect of grain-boundary misorientation on dynamic recrystallization of Cu-Si bicrystals, *J. Jpn. Inst. Met.* 58 (1994) 267–275. [doi:10.2320/jinstmet1952.58.3-267](https://doi.org/10.2320/jinstmet1952.58.3-267)
- [31] F. C. Ren, F. Chen, J. Chen, X. Y. Tang, Hot deformation behavior and processing maps of AISI 420 martensitic stainless steel, *J. Manuf. Process.* 31 (2018) 640–649. [doi:10.1016/j.jmapro.2017.12.015](https://doi.org/10.1016/j.jmapro.2017.12.015)
- [32] C. M. Sellars, W. J. M. Tegart, Hot workability, *Metall. Rev.* 17 (1972) 1–24. [doi:10.1179/imttr.1972.17.1.1](https://doi.org/10.1179/imttr.1972.17.1.1)
- [33] E. I. Poliak, J. J. Jonas, A one-parameter approach to determining the critical conditions for the initiation of dynamic recrystallization, *Acta Mater.* 44 (1996) 127–136. [doi:10.1016/1359-6454\(95\)00146-7](https://doi.org/10.1016/1359-6454(95)00146-7)
- [34] E. I. Poliak, J. J. Jonas, Initiation of dynamic recrystallization in constant strain rate hot deformation, *ISIJ Int.* 43 (2003) 684–691. [doi:10.2355/isijinternational.43.684](https://doi.org/10.2355/isijinternational.43.684)

- [35] M. S. Ghazani, B. Eghbali, G. Ebrahimi, Kinetics and critical conditions for initiation of dynamic recrystallization during hot compression deformation of AISI 321 austenitic stainless steel, *Met. Mater. Int.* 23 (2017) 964–973. [doi:10.1007/s12540-017-6391-8](https://doi.org/10.1007/s12540-017-6391-8)
- [36] G. K. Mandal, N. Tanford, P. Hodgson, J. H. Beynon, Effect of hot working on dynamic recrystallisation study of as-cast austenitic stainless steel, *Mater. Sci. Eng. A* 556 (2012) 685–695. [doi:10.1016/j.msea.2012.07.050](https://doi.org/10.1016/j.msea.2012.07.050)
- [37] A. M. J. Junior, O. Balancin, Prediction of steel flow stresses under hot working conditions, *Mater. Res.* 8 (2005) 309–315. [doi:10.1590/S1516-14392005000300015](https://doi.org/10.1590/S1516-14392005000300015)
- [38] C. Zhang, L. W. Zhang, W. F. Shen, C. R. Liu, Y. N. Xia, R. Q. Li, Study on constitutive modeling and processing maps for hot deformation of medium carbon Cr-Ni-Mo alloyed steel, *Mater. Des.* 90 (2016) 804–814. [doi:10.1016/j.matdes.2015.11.036](https://doi.org/10.1016/j.matdes.2015.11.036)
- [39] H. Mirzadeh, A. Najafizadeh, M. Moazeny, Flow curve analysis of 17-4 PH stainless steel under hot compression test, *Metall. Mater. Trans. A* 40 (2009) 2950. [doi:10.1007/s11661-009-0029-5](https://doi.org/10.1007/s11661-009-0029-5)
- [40] Y. V. R. K. Prasad, S. Sasidhara, *A Compendium of Processing Maps*. Materials Park, ASM International Press 1997.
- [41] Y. V. R. K. Prasad, Processing maps: A status report, *J. Mater. Eng. Perform.* 12 (2003) 638–645. [doi:10.1361/105994903322692420](https://doi.org/10.1361/105994903322692420)
- [42] Y. V. R. K. Prasad, Dynamic materials model: Basis and principles, *Metall. Mater. Trans. A* 27 (1996) 235–236. [doi:10.1007/BF02647765](https://doi.org/10.1007/BF02647765)
- [43] V. M. Sample, G. L. Fitzsimons, A. J. DeArdo, Dynamic softening of copper during deformation at high temperatures and strain rates, *Acta Metall.* 35 (1987) 367–379. [doi:10.1016/0001-6160\(87\)90244-6](https://doi.org/10.1016/0001-6160(87)90244-6)
- [44] A. Dehghan-Manshadi, P. D. Hodgson, Dependency of recrystallization mechanism to the initial grain size, *Metall. Mater. Trans. A* 39 (2008) 2830. [doi:10.1007/s11661-008-9656-5](https://doi.org/10.1007/s11661-008-9656-5)
- [45] G. Z. Quan, L. Zhao, T. Chen, Y. Wang, Y. P. Mao, W. Q. Lv, J. Zhou, Identification for the optimal working parameters of as-extruded 42CrMo high-strength steel from a large range of strain, strain rate and temperature, *Mater. Sci. Eng. A* 538 (2012) 364–373. [doi:10.1016/j.msea.2012.01.062](https://doi.org/10.1016/j.msea.2012.01.062)